Paper:

Liu, G., Cantó, J., Winwood, S., Rhodes, K. & Birosca, S. (2018). The effects of microstructure and microtexture generated during solidification on deformation micromechanism in IN713C nickel-based superalloy. *Acta Materialia*
http://dx.doi.org/10.1016/j.actamat.2018.01.062

The Effects of Microstructure and Microtexture Generated during Solidification on Deformation Micromechanism in IN713C Nickel-Based Superalloy

G. Liu[1], J. Salvat Cantó[1], S. Winwood[2], K. Rhodes[2], S. Birosca[1]

[1] Materials Research Centre, College of Engineering, Swansea University, Bay Campus, Swansea SA1 8EN, UK.

[2] Cummins Turbo Technologies, St. Andrews Rd., Huddersfield HD1 6RA, UK.

Abstract

Nickel-based superalloy IN713C produced through investment casting route is widely used for turbocharger turbine wheels in the automotive industry. The produced microstructure and microtexture are not homogeneous across the turbine component due to geometrical factors and localised cooling rate during the casting process, which give rise to inhomogeneous deformation during service. In the present paper, two kinds of in-house fatigue tests, Low Cycle Fatigue (LCF) and High Cycle Fatigue (HCF)， were conducted at 600°C in attempt to simulate the actual fatigue conditions experienced by turbine wheels in turbocharger. From Geometrically Necessary Dislocation (GND) distributions and strain analyses, it is concluded that microstructure heterogeneity such as carbide precipitates distribution within dendritic structure network determine the failure micromechanics during LCF tests. In the early stage of LCF loading, crack principally initiated within near surface carbides that have been oxidised during high temperature exposure. The higher GND density at the tip of carbide precipitates due to oxidation volume expansion are found to facilitate easy cracks initiation and propagation. Moreover, the cluster-like carbides network and its distribution can accelerate oxidation process and crack growth effectively. Furthermore, in the later stage of crack propagation during LCF, the weak interdendrite areas rotate to accommodate increased strain leading to faster cracks propagation and hence final catastrophic failure. Serial section technique for 3-D visualisation was employed to investigate crystallographic grain orientation correlation with fracture mechanics during HCF tests. It appears that the microtexure and grain orientations are more critical than the alloy microstructure in an area with a relatively uniform carbides distribution and weak dendrite structure where HCF failure occurred. Based on the slip trace analysis, it was found that most faceting happened in Goss grains (<110>//LD) and on slip system with the highest Schmid factor. It is concluded that cracks were initiated on planes with high Schmid factors and assisted by the presence of porosity.

Key words: IN713C; Fatigue crack; Oxidised carbides; Microtexture; GND.

1. Introduction

IN713C is a γ' precipitation hardened cast nickel-based superalloy that was developed by the International Nickel Company in the 1950s [1]. This alloy is still used in large quantities nowadays, because of its good castability, suitable mechanical properties and microstructural stability at elevated temperatures. However, IN713C alloys are mainly used in the form of precision cast parts for hot-end turbocharger wheels in the automotive and power generation industries. During investment process casting, the geometrical irregularity in turbine wheels shapes leads to disparity in solidification parameters such as cooling rate in different positions of the wheel component, which inevitably results in inhomogeneous microstructure and microtexture in the component. For instance, two different grain morphologies exist in the wheel blades, *i.e.* small equiaxed grains at blade tips and columnar grains in the bulk of the blades [2]. Furthermore, strain distribution inhomogeneity and localised deformation might be induced due to these microstructural inhomogeneities and finally affect the alloy’s performance and mechanical properties to different extend during service [2].

The turbine wheel blades are thermally and mechanically loaded during the operation of the turbocharger. The mechanical loading is caused by centrifugal forces and thermally induced mechanical loadings result from transient and inhomogeneous temperature fields within the blade. Conventionally, low cycle fatigue (LCF) and thermomechanical fatigue behaviour, which both may be significant during start-up and shut down of the engines, garner major research attention concerning the fatigue performance. In addition to the fatigue resulting from centrifugal force and wheel rotational speed during service, the fatigue caused by resonance is also found critical failure mode in turbine blade. In the later form, the high frequency of the blades may coincide with the wheel spinning at specific speeds (range), and cause 'VHCF (Very High Cycle Fatigue)'. In recent years, several works [3-7] concerning fatigue of IN713LC have been carried out to investigate the deformation behaviour and failure mechanism in both LCF [3] and HCF [3-5] conditions. Furthermore, Coleman et al., studied the microtexture correlation with turbine blade properties [2]. Most of these studies pay attention to defects in cast specimen [5], localised dislocation structure in small scale [6], and fracture surface analysis [7]. However, a comprehensive description of crack initiation and propagation is yet to be established for industrial benefit and scientific understanding. Moreover, the conducted experiments in the above studies used cylindrical button-end specimens from cast rods, which will inevitably result in a failure mechanism deviating from the real wheels, considering the geometrically complexity and inhomogeneous microstructure of the wheels and blades variation between the two.

In general, researchers agree that the major source of crack nucleation during fatigue test of nickel-based superalloys are casting defects such as porosity [5], inclusions such as carbides [8, 9] and persistent slip bands (PSBs) formation. For alloys subjected to high temperature fatigue loading, crack initiation in terms of surface oxidation and stress assisted intergranular oxidation have received considerable academic attention [10]. In particular, since fatigue cracks initiated by oxidised carbides were observed by Connolley *et al.* [11], the importance of carbides oxidation has been reported [12] and its effects on local lattice and chemical changes in adjacent areas have been studied in detail recently in [13, 14]. However, with the advancements in materials processing techniques and heat treatments, cast defects have been reduced and their influence on the fatigue life have been greatly minimised. Consequently, the roles of microstructure, grain boundary characteristics and local texture have subsequently become predominant factors in crack initiation and propagation [2, 15]. Moreover, it vital to study local plastic and/or elastic strain distributions as well as lattice distortions near specific features, if the deformation mechanism are to be well understood from a fundamental level. For these purposes, Transmission Electron Microscopy (TEM) and X-ray or neutron diffraction have been widely utilised but with their own shortcomings in length scales. However, by means of high-resolution Electron BackScatter Diffraction (HR-EBSD) which developed rapidly in recent years, it is possible to capture lattice distortions and dislocation arrangement at the mesoscopic and microscopic length scales, thus bridging a balance between analysis of individual defects in TEM and volume-averaged densities via X-ray methods. In particular, local changes in the lattice orientation reflect lattice curvature and can be further used to calculate Geometrically Necessary Dislocation (GND) densities. This type of calculation and measurement by means of HR-EBSD have contributed greatly in better understanding of dislocation arrangements in intra/inter grains [15, 16] and within local microstructure features in nickel-based superalloys. For instance, Birosca *et al.* [15] proposed distinctive dislocation evolution models in soft and hard grains based on the GND distribution in RR1000 superalloy during thermo-mechanical fatigue. Karamched *et al.* [17] first reported high resolution strain and GND distribution around carbides after heat treatment and deformation in a solidified superalloy. Britton *et al.* [18] confirmed the pile-up of dislocations at the intersection of slip bands and grain boundary, and further validate a dislocation mechanics by revealing elastic stress state ahead of the pile-up. By utilising HR-EBSD and/or High Resolution Digital Image Correlation (HR-DIC) technique, Jiang *et al.* [19, 20] revealed a direct relationship between dislocation density and fatigue crack nucleation in nickel-based superalloy containing non-metallic inclusions. Thus, HR-EBSD seems to be a promising tool in understanding the relationship between strain inhomogeneity, orientation gradients and GND accommodations as well as their interactions with microstructures during plastic deformation.

In the present study, in-house LCF and HCF (caused by resonance) tests are applied to real turbocharger wheels. Detailed post-mortem analysis including fractography, microstructure and microtexture characterisations of failed areas have been conducted. Moreover, the relationship between deformation micromechanism and microstructural heterogeneity has been investigated utilising HR-EBSD. The theoretical models of failure mechanics during LCF and HCF conditions are established throughout this study.

2. Experimental Procedures and Material Used

The turbocharger wheels produced via investment casting route were tested using Cummins in-house fatigue testing machines at Cummins Turbo Technologies Ltd/Huddersfield/UK. The tested turbine wheels were made of IN713C with a chemical composition shown in Table 1. An example of a general condition and geometry of the turbine wheels prior and post testing are shown in Fig. 1a and 1d, respectively. The wheels subjected to both LCF and HCF loading conditions. However, using in-house testing method the exact condition of LCF and HCF are slightly different from standard fatigue test as it is described below. Here, during the test the focus is on crack initiation, path and propagation and final fracture of the alloys rather than the total number of cycles to failure. The design of the LCF test here is based on the crack initiation from a high stress concentration points either at the surface, subsurface or in the bulk of the material. Whilst, the HCF test is designed to emulate the resonance effect on the blade failures. As shown in Fig. 2a, a standard turbine wheel housing is used for both LCF and HCF tests with the wheel connected to a controlled high rotating speed motor. The end of the housing is connected to an environmentally controlled chamber to supply a gas stream to the turbine housing. The inlet gas temperature in both tests was 600 °C. During the LCF test, the wheels were rotated with a wide speed ranges with maximum speeds above 100 krpm. Fig. 2b shows a typical

LCF speed cycles during the in-house test. From the same figure, it appears that tension-tension LCF loading condition is applied in such a test. The cyclical loading caused by the applied centrifugal stress to the turbine blades result from the ever-changing speed of wheels during the LCF test. It is estimated that induced centrifugal stresses that cause the alternating loading are generally below the yield strength of IN713C alloy, but with the presence of stress concentration local yielding may occur in specific regions of the wheel. A typical turbine speed versus time figure during HCF tests is shown in Fig. 2c. For HCF tests, by changing the wheel blade speed cycle/range and the inner housing structure, a 'push-pull' force is introduced around the tip of blades. when the push-pull forces occur at a rate that matches the resonant frequency of the blade, the blade will accumulate fatigue damage at a very high rate. The speed range for the test is chosen so that all blades will experience resonance during a half cycle.

Following the fatigue tests, the failed specimens were cleaned by ultrasonic bathing in detergent solution for 20 minutes and then in ethanol for 20 minutes in order to optimize fracture surfaces feature observations. Fracture surface study was then carried out for the failed blades using Keyence light microscope and Zeiss (EVO) Scanning Electron Microscope (SEM). The failed blades were then mounted and the surface parallel to loading direction (radial direction) metallographically is prepared. The standard procedure was followed for the sample preparation, culminating with 0.05 μm Colloidal Silica for 20 min. For further microstructure observations, the specimens were etched in Kalling's No. 2 solution (5g $CuCl_2$, 100 ml hydrochloric acid and 100 ml ethanol). After complete fracture surface characterisation, sectioning of failed fatigue samples was performed in order to observe regions surrounding crack initiation sites. This allowed complete characterisation of critical microstructure features controlling fatigue crack initiation and the early stage of small crack growth. Metallographic sectioning planes were parallel to TD-LD plane (Fig. 1b) and the loading axis in both LCF and HCF failed samples. Moreover, for HCF failed specimens, serial sectioning was also conducted across fracture surface (parallel to ND-LD plane) to reveal three-dimensional view around the cracked areas. Following each high-resolution imaging and EBSD scanning on each section surface, the mounted samples were then demounted to locate the exact location of the sectioning surface that has been characterised. High resolution imaging and EBSD were performed using a JEOL 7800F field emission gun SEM equipped with AZTEC data acquisition and analysis software and a Nordlys EBSD detector. To optimise the image or diffraction patterns quality, the SEM operating voltage used was 10~15 kV for imaging and 20 kV for EBSD scan with a current of ~ 14nA. A binning of 4×4 and Hough resolution of 85 were chosen to balance the time consumed and quality required, leading to an exposure time of 150 ms per pattern. The EBSD date analysis was conducted using standard HKL-EBSD Channel 5 software package.

The concept of GND originally based on the assumption that during plastic deformation, a strain gradient necessitates the creation of minimum dislocation networks to maintain the geometric continuity of the material [21]. This strain gradient often is produced in materials that have two phases that have different deformation ability or adjacent grains with different orientations in polycrystalline alloys [22]. The strain gradient results in orientation gradient and the later can be derived from misorientation across grains, thus the ability of probing orientation of grains in EBSD making the calculation of GND density across grains possible. The detailed mathematical description of GND is given by Arsenlis and Parks [23]. The basic equation for this calculation is dislocation density tensor α_{ij}, which quantifies the content of dislocations in the lattice was:

$$\alpha_{ij} = \sum_{t} b_i^t \, l_i^t \delta(\vec{x} - \overrightarrow{x^t}) \quad (1)$$

Where Burger vector $\vec{b}$ characterise the displacement, dislocation line vector $\vec{l}$ indicates their direction, t denotes the type of dislocation and position vector $\vec{x}$. In the present study, we use a Python code to calculate GND which is reported in detail previously [15]. First the Euler angles were converted to a quaternion unit for each point, which were further used to calculate misorientation quaternion. It is worth noting that the misorientation quaternion is calculated for each point along with its adjacent neighbour rather than central point of the grain. Then misorientation vector maps can be obtained, from which only five out of nine Nye dislocation tensor components can be derived as only 2D EBSD orientation date are available. For each type of dislocation from the 18 types of dislcoations in fcc crystal, we use a combination of five Nye components to resolve at each point and thus, different combinations of dislocation types are selected to solve the equations. The sum of the absolute values of all components of the dislocation density tensor yield the total dislocation density [24]:

$$\rho_{gnd}^{tot} = \frac{1}{b}\sum_{i=1}^{3}\sum_{j=1}^{3}|\alpha_{ij}| \qquad (2)$$

from which the minimum total GDN density was chosen.

In the current study, the step size of EBSD mapping used for GND calculation varied from 60 nm to 300 nm as well as 0.5 micron in order to balance between the microscopically relevant and EBSD noises. It should be noted here that the error in dislocation density calculation will increase as the step size decreases [25, 26]. For the GND calculation in IN713C, a Burgers vector value of **b** = 0.254 nm was used [27]. All GND maps were plotted in logarithmic scale and total dislocation density per μm^2 unit area was used for GND measurements in this study.

For HCF failed specimen, slip trace was also determined in faceted and surrounding grains around crack initiation sites. From the crystallographic orientation data acquired by EBSD, the slip plane traces angle with LD were calculated. In the present study, we aligned the blade LD with the SEM *Y*-axis when inserting the sample into SEM chamber, see Fig. 1b and used the sample reference of *X*-axis = ND (note that the cross section is used for calculation), *Y*-axis = LD and *Z*-axis = TD. Following the quaternion conversion of Euler angles as mentioned above, all possible (111) slip plane traces then can be calculated using the cross product of the slip plane normal and the surface normal. Furthermore, the Schmid factors for each grain were calculated with Eq. (3):

$$S^{\alpha} = (gl \times n^{\alpha})(gl \times S^{\alpha}) \qquad (3)$$

where (g) is the orientation of each grain, (l) is the loading axis, n^{α} is the unit normal to the (111) slip planes and s^{α} is unit slip direction along <1-10>, in which α =1, 2, …12. Following this calculation, the angle between the slip trace and the unit LD (l) is determined by [28]:

$$Angle(°) = cos^{-1}[(gm \times \bar{n})\times(gl)] \quad (4)$$

where $\bar{n}$ is the slip plane normal and m is the free unit normal. The detail of both GND and slip trace determination can be found in [15].

3. Results

3.1 Fractography Observations

In the current study fractography, *i.e.*, fracture surface study, was used to identify the main difference between LCF and HCF fracture surface features. Fig. 3 and Fig. 4 both give three representative examples of fractographies of HCF and LCF samples after failure, respectively. Macroscopically, nearly all HCF failures occurred in the upper position of blades, see Fig. 1b and it appears that the fatigue failure occurred following three stages, as indicated in Fig. 3a and magnified in Fig. 3b-d, *i.e.*, Stage 1: crack initiation on a specific grain plane, see Fig. 3c; Stage 2: relatively flat and large crack propagation area with characteristic of striations, see Fig. 3b and d; and Stage 3: tensile overload area which suffers catastrophic mechanical failure with ductile fracture features (dimples). The other two examples are shown in Fig. 3e-f and g-h, respectively, showing the same three failure stages as in Fig. 3a-d. Although the same faceting phenomenon had occurred in stage 1 in all the specimens, the crack initiation sites were differed. The crack sometimes was initiated in the vicinity of casting defects such as porosity (Fig. 3c) or inclusions (Fig. 3e, f), or from the sample surface as shown in Fig. 3g. In Fig. 3g, another characteristic of fatigue, beach marks, can also be clearly seen on the facet plane.

For LCF cases, the failure occurred on the blade root, see Fig. 1c. The predominant features in LCF failed samples are (1) dendrite structure as indicated in Figs. 4a and 4b, and (2) secondary cracks as indicated in Fig. 4c, both of which are close to initiation sites, indicating that the dendrite structure play an important role in crack propagation, as once the crack initiated during LCF, it can propagate in other directions depending on the dendrite morphology and structure. Moreover, the microstructurally crack propagation areas were not clear on the fracture surface, see Fig. 4e. In other words, there was no clear transition between crack propagation area and tensile overload area as was observed for HCF. This might indicate a faster crack propagation during LCF than in HCF. Microscopically, in HCF samples, long continuous striations, which are the most eminent features of fatigue can be found in the propagation areas, especially at the end of crack propagation areas, see Figs. 3b and 3d, and this is in agreement with most striations observations [29]. Although no such long and continuous striations was found in LCF samples, many local striations with different directions can be clearly observed in the propagation area, see Fig. 4d. Moreover, oxidised striations were also observed near crack initiation site, see Fig. 4f. It appears that the most contrasting difference between HCF and LCF is that the initiation sites in HCF is highly orientation dependent. Although most of cracks in HCF samples initiated directly from casting defects such as pores (Fig. 3c) and inclusions (inset of Fig. 3f) which are stress concentration locations, they are all located in grain planes with specific orientations. These planes on the surface of which feature with cleavage fractures are generally known as ‘facet’, are not unusual to be observed in HCF failed specimens. It is generally believed that the facet planes possess a specific angle with loading direction that favourable for slipping during external loading. As shown in Fig. 3g, not only did the crack start from a facet, but the propagation of crack also depended on specific oriented planes (indicated by blue arrows in Fig. 3g with one of area enlarged in Fig. 3h). Further microanalyses show that the dendritic structure and secondary cracks are found close to crack initiation site in LCF failed specimen, see Fig. 4b, which is rare case in HCF sample and this aspect will be further investigated in the next section.

3.2 The Effect of Blade Geometry and Local Microstructure on Crack Initiation Site during LCF and HCF failures

The microstructure of cast IN713C generally consists of dendritic structure with MC type carbides that are rich in Nb, Mo, Ti trapped within interdendritic channels [1, 30]. For turbocharger wheel blades produced via investment casting, the irregular geometry give rise to different cooling rates and thermal gradients, that leads to further microstructure disparity in different locations within the wheel blades. Fig. 5 shows the microstructures of the failed blades during both LCF, close to blade root, see Fig. 5a-d, and HCF, upper position of the turbine blade, see Fig. 5e-h. As can be clearly seen in the figures, the major differences lie in the dendritic structure, as well as the size, morphology and distribution of MC-type carbides. Based on high resolution EDS analysis used in the current study, all the carbides throughout blades have the stoichiometric ratio of $(Nb_{0.7}Ti_{0.2}Mo_{0.1})C$, which is in agreement with previous reports [1, 30]. It is well established that Mo and Ti generally partition in γ and they are carbides formers. However, unlike Mo and Ti, Nb is mostly diffused and segregated in MC carbides, making Nb-rich carbides all along the interdendritic areas. Based on this consideration, the Nb EDS map was used to identify the carbides location and their distribution as well as to reveal the dendritic structure. As shown in Figs. 5b and 5f, almost all the carbides precipitate in interdendritic areas, except a few numbers observed along γ grain boundaries. It is evident form Fig. 5a-d that the dendrite structure is more apparent with wider primary and secondary arms in the area where LCF occurred. Whereas finer primary arms were observed in the areas where HCF occurred, see Fig. 5e-g. Moreover, well defined and characteristic secondary arms can be clearly seen in the area where LCF occurred, see Fig. 5b. These microstructure characteristics indicate a faster cooling rate and/or a high thermal gradient exhibited in upper location of blade where HCF failure took place.

In general, the carbides chemical composition and their trapping in interdendrite channel were the same in the locations where LCF and HCF took place. It is clear from Figs. 5c and 5g that the carbides show Chinese script and cluster morphology in the area where LCF failure occurred. Whilst the carbides show more uniform and granular shape in the area where HCF failure occurred. Although it is difficult to quantitatively analyse carbides size and their distribution due to the connectivity in 3D of some carbides (particularly in LCF sample), it is obvious that carbides in LCF specimen are much larger in size than that in the HCF specimen, with 5~40 μm in the former and 1~10 μm in the latter. Despite the obvious difference in MC carbide size and shape, the total volume fraction of carbides in two locations are almost the same with 1.8%, which seems less affected by cooling conditions. The effects of cooling parameters on microstructure including carbides and dendrite in casting superalloys have been widely studied. The shape and size of carbides in IN713C was reported depend on solidification parameters such as thermal gradient, growth rate and local cooling rate where a higher cooling rate leads to finer carbides size [30]. It is worth noting here that besides the disparity in carbides size and morphology, the connectivity of carbides clustersin LCF specimen as mentioned earlier, see Fig. 5c, might affect the low cycle fatigue property, which will be discussed in Section 4.2.

3.3 Near-Surface Carbides Oxidation and GNDs Heterogeneous Distribution in LCF Failed Specimens

Detailed microstructure observations revealed a prevailing oxidation phenomenon of carbides close to fracture surface in LCF failed specimen as shown in Fig. 6. The EDS mapping of carbides and oxides in the inset of Fig. 6a clearly identify that some $(Nb_{0.7}Ti_{0.2}Mo_{0.1})C$ carbides in the vicinity of specimen surface had been oxidised. The oxides share a similar stoichiometric composition with carbides as $(Nb_{0.7}Ti_{0.2}Mo_{0.1})O$. Furthermore, semi-oxidised carbides were also found near the failed sample surface, see Fig. 6c, d. It is evident that the oxidation process initially started from the centre of carbide precipitates, see the same EDS maps for Fig. 6d. Fig. 6 clearly demonstrates that oxidised carbides can play a vital role in secondary cracks formation and its behaviour, causing secondary crack deviation and undulation, Fig. 6a; forming new secondary cracks, Fig. 6b; initiating short (inner) cracks within γ matrix, Figs. 6c and 6d. It should be noted that in addition to the stress assisted intergranular oxidation [10], these types of near-surface carbide oxidation and their effects on fatigue property received scientific attention recently in single as well as polycrystalline superalloys that contain high content of Nb during high temperature exposure [11-13]. It is suggested the tensile stress resulted from volume expansion of carbides oxidation leads to the short crack initiation [11]. However, as clearly shown in Figs. 6c and 6d, all the small initiated cracks are perpendicular to the loading direction, indicating the stress assisted effects on short cracks initiation within the oxidised carbides. From current investigation, it is established that carbides are brittle precipitates and can act as preferable sites of crack initiation. However, they are less susceptible to cracks than the oxidised carbides.

Fig. 7 shows continuous carbide and oxide along a short crack. It is clear from EDS maps (O, C, Nb, Fig. 7b-d) that only the carbides within the opened crack were oxidised, see the non-oxidised carbide away from the crack in the white dashed ellipse shape on Fig. 7a and 7d. It shows that the short cracks initiated at the tip of oxidised carbides and perpendicular to the loading direction. Figs. 7e and 7f show EBSD-derived IPF//LD map and GND map, respectively. Form the IPF map the carbides as well as oxidised carbides along the crack are all within one big grain. From the same figures, it appears that the carbides have slightly different orientation from the γ matrix, see the white dashed ellipse in Fig. 7e. It appears that carbides have an FCC crystal structure and similar lattice parameters to γ matrix. This is in good agreement with the Transmission Electron Microscope (TEM) observation in [1]. Looking at the GND density distribution around the oxidised carbides in Fig. 7f, it is not surprising to find higher GND density around oxidised carbides. This is due to different deformation behaviour, hardness and volume expansion coefficient between carbides and the γ matrix that cause strain heterogeneity and GND accumulation. However, it is clear that the GND density at the end of oxides (where small cracks initiate) and ahead of the cracks (see the rectangular areas 1, 2 in Fig. 7f) are much higher (about two orders of magnitude) than those in the γ matrix. It seems the GND accumulation along crack direction or perpendicular to the loading direction. Moreover, it is safe to assume that high GND density ahead of the small cracks can promote further propagation.

To investigate carbide and oxide connectivity as well as secondary and primary crack networks within the bulk sample, a three-dimensional imaging was performed using layer-by layer grinding and polishing method. Fig. 8 shows only 3 sections of the 3D observation: LD-TD plane surface in Fig. 8a which is the same plane surface in Fig. 7a, 20 and 40 microns away from the surface in Fig. 8c and 8e, respectively. The micro-crack in Fig. 8a appear as an isolated crack within the bulk sample, however, looking at other sections in Fig. 8c and 8e, it is evident that the crack was connected to the primary surface crack. This 3D connection provided sufficient oxygen amount to be diffused from the sample surface to deep inside the material in order to oxidise the carbides during 600°C fatigue test. Moreover, it is evident that the small crack shown in the inset of Fig. 8a grew along the oxide/carbide boundary with the carbide been continually oxidised along the crack. This is because the oxide/carbide was directly bordered by a γ', see the black dashed rectangular area in Fig. 8a and enlarged in Fig. 8d, and the crack was finally arrested when it encountered by γ', however, after leaving a large GND accumulation at the tip of the crack which indicates strong γ' resistance to crack propagation, see Fig. 8b.

Further investigation was carried out in order to obtain a comprehensive description of carbide and oxide effects on crack formation and propagation in LCF and HCF failed specimens. For the statistical reliability purpose a large number of individual carbides (~ 100) in a depth of 200 μm away from the fracture surface and close to initiation sites were analysed by means of EBSD and GND density calculations. As shown in Fig. 9a-c, 21 carbides are identified in the LCF failed specimen with size ranging from 0.5 to 11 μm and large strain accommodation around them. It is clear from the EBSD-derived IPF//LD map in Fig. 9b that some of the carbides have completely different orientation from γ and γ' phases, *i.e.*, γ has a <112>//LD orientation while most carbides have <110>//LD and some close to γ orientation. Furthermore, the strain heterogeneous distributions are quantitatively analysed as shown in GND density map in Fig. 9c. It is clear from the GND map that higher GND density was observed surrounding areas of carbides, due to the different deformation behaviour between carbides and matrix during loading. The high GND density on carbides/matrix boundaries is more related to plastic strain incompatibility between the γ matrix and MC carbide, where these two phases were strain hardened in different rate and level during deformation. However, care should be taken when dealing with the concept of strain hardening where another type of dislocation, *i.e.*, statistically stored dislocation (SSD), that can also contribute in strain hardening is not measured here. It is well established that SSD evolves from random trapping processes, and GND is correlated to lattice curvature [15-16, 21-23]. A closer observation in the current study suggested that the high GNDs around carbides were not uniform. This observation was more evident in the IPF map in Fig. 9b. As shown in the figure, the white areas indicated by arrows correspond to high GND density in Fig. 9c. This GND accumulation is partly due to the shape and sharp edges of carbides, see carbide 10, 12, 20 in Fig. 9b. Furthermore, the loading conditions might have a direct effect on this type of GND accumulation, see carbides 1-4 in the same figure. Further analyses showed that the high GND density also exist in areas away from carbides (indicated by blue arrows in Fig. 9c). Considering the 3D network of carbides distribution mentioned above, it appears that these extra high GNDs reflect the strain accommodation surrounding the tip of carbides just below the current observed surface. In contrast to the high GND density surrounding carbides in LCF, the GND density map for HCF shows low density variation around carbides in upper position of blades failed during HCF test, see Fig. 9e and 9f. Similar GND measurements around carbides were performed by Karamched and Wilkinson [17] on a high Ta-containing directionally solidified Ni based superalloy. They found that the average GND density around carbides increased with increasing applied strain levels during three-point bending test. They also argued that this increase is slightly attributed to the pre-existing plastic residual deformation caused by thermal mismatch between carbide and nickel matrix [17]. However, the thermal mismatch appears to have little effect on the GNDs density in the present study as no obvious increases in GND density was evident between carbide and γ matrix, see Fig. 9f. On the other hand, by comparing the GNDs density in LCF and HCF, see Fig. 9c and 9f, respectively, it is clear LCF are imposed higher strain than in HCF, with average GNDs density of order of $10^{3.8}$ μm^{-2} (6.3×10^{3}) around carbides in LCF while ~$10^{2.4}$ μm^{-2} (2.5×10^{2}) in HCF.

It was interesting to note that the GND density within carbides was much less than the GND density in the surrounding areas, for instance, see carbide number 5, 7, 8, 10, 12, 21 in Fig. 9c. It appears that

GND density in the carbide was slightly less than the average GND density of γ matrix, which indicates in the hard and brittle nature of carbides. The reduced ductility of carbide lead to inhomogeneous deformation and less strain accumulation, hence less dislocation generation during LCF loading. It should be emphasized here, that during HCF loading, the GND density within the carbides seems to be rather uniform with the rest of matrix, see Fig. 9f. This is mainly due to overall lower GND density of γ matrix in HCF failed sample which were exposed to less straining during HCF loading. However, in general in both LCF and HCF cases, the carbide contained much less GND density than the matrix.

Further GND measurement was conducted to investigate the GND density and their distribution in the dendrite structure within large area of the blade. Fig. 10a-b show the GND density in a large area for the same LCF failed specimen as in Fig. 9a-c. The plane area of interest in both Figs. 9a and 10a was parallel to LD-ND plane, which was parallel to main crack propagation direction of the primary crack, see also Fig. 1c. It is obvious from Fig. 10a-b that the dendritic structure has a great effect on the GND density distribution in LCF. The figure shows much higher GND density in interdendrite area (averagely $10^{3.7}$ μm^{-2}) than in dendritic area (~$10^{2.3}$ μm^{-2}). This GND density disparity imply the heterogeneous strain accommodation caused by the dendrite structure during plastic deformation. These dendrite structures are generated during the investment casting solidification process. However, essentially, they are the consequence of microsegregation of the alloying elements at the solidification front. Fig. 10c shows the EDS mapping of six major elements in the material in local dendrite/interdendrite structure. It is clear from the images that Ni and Al enriched and partitioned in dendrite area while Cr, Mo, Nb and Ti enriched in interdendrite areas. Moreover, among the latter four elements, only Cr uniformly distributed across the entire interdendrite area and did not diffuse or segregate into the carbide precipitates, see Cr EDS map. Whilst large quantity of Nb, Ti and Mo are merely partitioned and segregated into MC-type carbides. However, Mo shows a slightly wider diffused area in the EDS map compared with Nb and Ti segregation in carbide. The segregation ratios, defined as the maximum concentration in interdendritic areas over minimum concentration in dendrite core for each element, are determined and shown in Table 2. Fig. 10d shows a typical example of dendritic structure in the crack propagation area in the LCF failed sample. Moreover, secondary cracks can also be found along the dendritic structure. These prevailing dendritic structure along primary cracks and secondary cracks along dendritic structure clearly signify the weakening effect on LCF properties and this effect closely related with the heterogeneous strain distribution that identified by GND measurements.

3.4 The Effect of Grain Orientation on Crack Formation and Propagation during HCF Loading Condition

The microstructure of fracture location following HCF tests including the dendritic structure, carbides distribution and morphology as well as GND density across the sample were performed and compared to LCF failure mechanism. It is demonstrated in Section 3.1 that faceted fracture nature was exhibited at the initiation site in HCF failed blades. In this section, we mainly focus on the effects of microtexture and grain orientation on crack initiation and propagations using serial sectioning across and around the facets on the fracture surface. After each sectioning, secondary electron (SE) images were taken to precisely locate the actual section positions on the fracture surface plane. Fig. 11 and Fig. 12 show the orientation and grain size/shape distribution across the fracture surfaces in two typical HCF failed blades. The fracture surface shown in Fig. 11 is the same one as in Fig. 3a in which crack initiated from a porosity. The topographic features in Fig. 12a are very similar to those in Fig. 3g and crack initiated from blade surface. Both serial IPF//LD along cross section, *i.e.* parallel to LD-ND plane, see Fig. 11d-f and Fig. 12b, and IPF//LD along profile, *i.e.* parallel to LD-TD plane, see Fig. 11b and Fig. 12b-c, are illustrated to give a comprehensive view of the grain orientations and grain distribution near the failed areas. The critical points, *e.g.* grain boundary along section lines are also indicated by numbers or letters in red in fracture images and IPFs, see Fig. 11c-f and Fig. 12a-c. It can be clearly seen that these HCF failed blades consist of large grains, with 2 or 3 grains along

ND and 1~3 mm along LD. In the first example, the crack initiated and facet formed in the Goss grain (<110>//LD), and the facet ended at the grain boundary, see points 3 and 2 in Fig. 11c, d. The same situation applies to the second example, where facet also formed in a Goss grain, which is roughly circled by points D-E-I-M-L, see Fig. 12a, b. The facet also ended at the encountering grain boundary, see points I and E in Fig. 12a, e, f. The results clearly show that facet area correspond well with the grain size.

As shown in Fig. 11e and Fig. 12d, the (111) slip traces are superimposed on IPFs, and Schmid factors for each slip systems in facet grain (Goss grain) are also calculated and presented. These figures show that facet plane is parallel to the slip plane with highest Schmid factor among all slip systems available, *i.e.* (11-1) [1-10] in the first sample and (1-11) [10-1] in the second sample, see the slip trace line in red in Fig. 11e and Fig. 12d, respectively. It should be noted here that the highest Schmid factor in the faceted grain in Fig. 11, although already high with 0.45, is slightly lower than the one in Fig. 12 (0.49). Since the first facet initiated from a pore while the second one started from surface, it is reasonable to deduce that the stress concentration induced by porosity might reduce the critical sheer stress needed for slip system activation. In other words, when Schmid factor is high enough, the slip of that plane can occur without an assistant of the presence of defects such as porosity or inclusions. The angle between the facet and horizontal plane (TD-ND plane) are around 35° in both cases. The degree of deviation of faceted grain away from ideal Goss orientation are determined using ODF (Orientation Distribution Function), and shows ~7° away from ideal Goss in the both cases, representatively shown in Fig. 12e. For crack propagation stage in the first HCF fracture surface, where featured as visible striations, propagation area was found within the same Goss grain, although changed into different lattice planes after faceting, see Fig. 11. Whilst for the second fracture surface, after faceting in Goss grain ‘H-I’, fatigue crack further propagates in adjacent grain ‘I-J, E-F’. In this fractured specimen, Schmid factors of two other surrounding-faceted grains have also been calculated and listed in Fig. 12f. It shows that neither the highest nor average values of Schmid factor for the two grains are lower than that in the faceted grain, especially in Brass grain (grain 3), in which two of four available slip systems were almost zero. The low Schmid factor of the grains indicate on unfavourable crystallographic orientation to activate {111}<110> slip system. The different values of Schmid factor together with the grain size and distribution are believed to have great effect on the crack initiation and propagation during HCF as will be discussed in the Section 4.

4. Discussion

4.1 On the Role of MC Carbides and MC Oxide in LCF Deformation Mechanism

It is demonstrated in Section 3.3 that MC carbides in IN713C alloy plays a vital role in determining the LCF properties. It was also observed that the MC carbides' size, shape, edges and prevailing precipitation distribution across γ matrix as well as their coherency and different deformation nature from γ have a great influence on LCF failure mechanism. On the one hand, as a second phase particle, carbide strengthen IN713C via precipitate strengthening by resisting dislocation motion (both SSD and GND) and dislocation fostering (Fig. 9c). On the other hand, when the strain that is resulted from heterogeneous deformation between carbides and matrix is accumulatively sufficient, can lead to carbides cracking, see the arrows in Fig. 5d and Fig. 9a. This is one of the major source of small crack formation and micro crack propagation as found in the centres of the brittle MC carbides.

It is clear that the most deleterious effect of carbides on fatigue property is observed upon their transformation to oxides. Connolley *et al.* [11] estimated the volume expansion factor between Nb_2O_5 and NbC may varies from 2 to 2.4. The volume expansion factor is defined as: $\delta_{\mathrm{V}} = \frac{V_{\mathrm{Nb_2O_5}}}{2V_{\mathrm{NbC}}}$. As stated earlier the composition of carbides in the current study is found to be complex stoichiometric formular of $(Nb_{0.7}Ti_{0.2}Mo_{0.1})C$. However, the volume expansion due to different volume expansion coefficient in carbides and oxides is highly expected during carbides oxidation. It has been also reported that in stress free condition prior to deformation, sub-surface carbides can readily be oxidised with a characteristic surface eruption. It is also claimed that this type of oxidation process can lead to a localised γ deformation around the oxidised carbides [11]. This type of local deformation of γ matrix is mainly induced by the volume expansion during carbides oxidation. This volume expansion-induced localised deformation during phase transformation also have been reported in other alloys [16], for instance, the volume expansion during austenite-to-martensite transformation in dual steels that cause adjacent ferrite matrix to deform [16]. Surface carbides oxidation has also been studied by Reed *et al.* [13] recently when comparing the different effects of MC carbides and M_5B_3 borides on tensile property of a nickel-based superalloy at elevated temperature. In addition to surface eruption and volume expansion, pores around oxidised carbides have also been observed by them and supposed to cause microcracks. The similar observation of higher GND density around cross-sectioned oxidised carbides has been made by Kontis *et al.* [14] recently. They also reported suspected softer area of recrystallization adjacent to oxidised carbide and caused by elements diffusion through dislocations, which might also contribute to the weakening of oxidised carbides areas [14].

In general, during deformation, geometrically necessary dislocations (GNDs) are required for maintaining lattice continuity [21, 22] and statistically stored dislocations (SSDs) evolve from random trapping processes. However, except at the tip of long oxidised carbides, it appears there is no significant GND density increase was found around oxidised carbides compared to the GND density around the non-oxidised carbides, see Fig. 9c and Fig. 7f. Considering the long irregular script-like shape carbides in LCF failed specimen (Fig. 5c and 5d), it is likely that the volume expansion and stress accumulation near MC and MC oxides mainly occur in the high geometrical curvature sites such as the edges and the tip of carbides parallel to the loading direction. Moreover, it appears that the volume expansion may not cause a uniform deformation near oxidised carbides in all directions, but instead, the generated strain, hence stress, parallel to the external loading axis, caused a localised deformation in the geometrically weak sites and could lead to microcracks initiation. It should be noted here that the geometrically weak site is refers to carbide edges and corners. After such transformation-induced deformation, residual stresses remain due to the inhomogeneous plastic deformation and can further facilitate crack growth. The non-uniform and inhomogeneous distribution of GNDs around carbides in all directions is demonstrated in Section 3.3 and shown in Fig. 9c. This phenomenon is also reported in [17], where sharper corners tend to possess higher density of GNDs than the curved corners. In order to study the inhomogeneous distribution of effective strain and GNDs around non-metallic inclusion, an elastic finite element (FE) model has been generated and suggested that geometry of inclusion is responsible for the stress/strain conditions and hence GNDs accumulation in different directions [17].

Recently, GND concept is used widely to understand the deformation mechanism, strain hardening and recrystallization in various materials such as pure copper [31], titanium [18] and nickel-based superalloys [19]. It has also been reported that there is direct correlation between high GND density and LCF crack initiation and propagation in inclusion-containing superalloys [19, 20]. According to Stroh [32], the dislocation pile-up leads to crack nucleation as they increase the local shear stress which facilitates nucleation of a micro-cracks. However, it is argued that dislocations cannot be a sole criterion for crack initiation as high GND are not limited to crack initiation sites [19]. Based on the concept and evaluation of stored energy [33], the dual role of GNDs in fracture process was proposed by Jiang *et al*. [19]: On one hand, GNDs accumulation can lead to local hardening and increasing the critical resolved shear stress. The stored energy is therefore increased and their dissipation lead to crack nucleation; On the other hand, GNDs can foster ahead of cracks and may have blunting effect as driving force for crack growth decreases. Both effects of GNDs were observed in the present study. First, as shown in Fig. 7f, high GND density at the tips of oxidised carbides could initiate micro-cracks, and secondly, the blunting effect could be clearly observed by the formation of the GNDs wall ahead of the small cracks (see the two rectangular areas in Fig. 7f). It is therefore concluded that GND fostering and accumulation can be an indication of plastic zone formation at the tip of the crack, and/or represent a strong driving force for crack propagation during loading. Thus, the GND calculation and strain mapping should be carefully utilised in deformation mechanism study. Therefore, the authors of this study believe that the local plasticity and stress state should be considered to understand the contribution of GND on strain hardening and fracture mechanics.

Furthermore, GND density is not represent the total number of the dislocation as SSD cannot be measure or calculated by merely EBSD data. Thus, SSD contribution on dislocation fostering and accumulations should be also considered in this aspect.

Great attention in the current study was paid to understand the carbides oxidation and in particular, oxygen transportation through precipitate hardened IN713C alloy. In general, oxygen has limited ability for diffusion in nickle based superalloy [34], thus the lattice diffusion cannot be a major oxygen transportation channel for oxidation to occur. As proposed in Section 3.3 and shown in Fig. 8, the oxygen transportation was mainly through primary and secondary cracks that are formed during loading. Many observations supported this particular postulation in this study. First, all the LCF failure found in this study occurred on the surface of the blade root (Fig. 1c). Once the initial micro-crack forms, either under external stress or from surface oxidised carbides, oxygen can readily channel through the crack to sub-surface carbides, providing carbide network as discussed previously. Moreover, once the carbides have been oxidised, the MC oxides themselves can act as medium for further oxygen transportation. The connecting cluster-like carbides distribution shown in Fig. 5c can provide carbides bridging for oxygen transportation. Secondly, carbides oxidation was rarely found in HCF failed sample under the same temperature and testing condition. It appears that the dominant factor is that most of HCF cracks initiated inside the upper position of blades (Fig. 3). Thus, diffusion of oxygen through γ matrix shows negligible effect compared with the crack channelling on oxygen transportation as discussed earlier. In conclusion, it is well known that oxides are more brittle than carbides due to crystallographic nature, and together with the strain induced by volume expansion during oxidation transformation as described earlier, it is established that the oxidised carbides are much more susceptible to microcracking than carbides.

4.2 On the Role of Dendritic and Interdendritic Structure in LCF Deformation Mechanism

The interaction between individual carbides/oxidised carbides and small cracks discussed in previous section underline the damage mechanism at microscopic scale at the early stage of crack initiation and propagation. Macroscopically, however, these damage accumulations lead to the weakening of large interdendrite areas where accommodate most of carbides and might accelerates crack propagation afterwards. Fig. 13 illustrates such weakening of interdendrite and its effects on failure mechanics. The dendrite structure is shown in Fig. 13a with area of interest been indicated by red rectangular inset and higher magnification of the area of interest are shown in Fig. 13b and 13c. The dark contrast of interdendrtite area in the EBSD band contrast images, see Fig. 13b, indicate lattice distortion and high local misorientation in that area. IPF in Fig. 13e shows that the original grain has a Brass orientation (<111>//Loading Direction (LD)) while the interdendrite shows Cube orientation (<100>//LD). In general, Brass oriented grains are regarded as hard grains with low Schmid factors and hence the slip system is difficult to be activated. Therefore, grain rotation is necessary in order to accommodate further external strain. Clearly a lattice rotation indeed happened in the area studied, but instead of the rotation of whole Brass grain, only weakened interdendrite rotated, specifically, about 55° along <110> axis from Brass to near Cube orientation, see Fig. 13e. In other words, at this stage of crack propagation, during loading of hard Brass grains, only the interdendrite area was rotated toward a soft orientation, *i.e.*, Cube with higher Schmid factor (Fig. 13d) so that can facilitate an easy slip system activation and hence crack propagation. This type of local lattice rotation would eventually lead to grain fragmentation and fracture of the blade in this area. This is further demonstrated in Fig. 13c, where a crack formed at the dendrite-inderdendritic boundary. This is analogous to dislocation motion theory which replace the whole bulk shear during plastic deformation of alloys. The high GND density in Fig. 13f and severe deformed γ' in the interdendritic area shown in Fig. 13c as well as long cracks along dendrtite/interdendrite interface are the result from the lattice distortion and hard Brass grain fragmentation.

Based on the experimental observations discussed above, it is proposed that the failure of turbocharger wheel blades under LCF condition is followed a sequence of events as schematically drawn in Fig.14. It is reasonable to assume that prior to the LCF test, only a limited amount of SSDs and low density of GND existed around the large size carbides in the cast IN713C, see Fig. 14a. When the cast alloy subjected to LCF loading (cyclic centrifugal stress), large quantities of GNDs generated around carbides in order to accommodate the local strains as a result of heterogenous strain distribution, especially at the tip of carbides. As discussed earlier the tip represent geometrical irregular site that can be a preferential site of strain accumulation and dislocation fostering with a possibility of some carbides may crack due to inner stress, see the highlight in Fig. 14b and Fig. 9c. As cyclic loading continues, high stress concentration site at the blade root surface initiates small cracks (either by persistent slip band or surface carbides/oxidised carbides interface failure). Once the cracks form, oxygen can diffuse through the crack and readily oxidise the sub-surface carbides, which induce more GNDs at the tip of carbides due to volume expansion and lead to further crack propagation, see Figs. 14c and 14d. As oxygen continue to be channelled through oxidised carbides and cracks, the adjacent carbides would be oxidised along the crack length, see Fig. 14d. Considering the cluster-like and connecting structure of carbides distribution in the blade root area as shown in Fig. 5b, 5c and Fig. 10, this oxidation-crack-oxidation interaction are expected to continue consequently.

Fig. 14b-d show the early stage of fatigue failure microscopically. Moreover, in a larger scale, the effects of dendritic/interdendritic morphology as well as carbide network and distribution on deformation micromechanics during LCF loading is demonstrated in Fig. 14e. It is evident in the figure that interdendrite accommodate much higher GND density than in dendrite areas. As the damage accumulate further, at the late stage of crack propagation during LCF failure, the weakened interdendrite area will first rotate to accommodate increased strain and facilitate further crack propagation, see Fig. 14f, which lead to the blade failure via grain fragmentation process as discussed earlier.

4.3 On the Role of Grain Orientation and Grain Morphology in HCF Crack Initiation and Propagation Mechanism

The crystallographic facets observation on the crack surface plane in nickel-based superalloys have been widely reported and generally attributed to the slip behaviour on {111} slip system in materials with FCC crystal structure during loading [4]. In the present study, facets have been found not only in grains with orientation of near Goss (<-101>//LD) as shown in Fig. 11 and Fig. 12, but also in Cube (<100>//LD) and Copper (<112>//LD) orientation grains. Table 3 shows Schmid factors of all the 12 slip systems in these grains including Brass (<111>//LD) oriented grains for comparison purposes. Illustrations of {111}<110> slip systems with some highest Schmid factor values in the ideal Cube, Goss and Copper orientations are shown in Figs. 15b, 15c and 15d, respectively. In the figures, the plane of (-111)[101] slip system is indicated in green and slip direction in blue. The red planes shown in the same figures are the perpendicular planes to the Loading Direction (LD) in each of the ideal orientations studied here. For instance, in Goss grain, the angle between loading direction and slip plane normal is 35.25°, see Fig. 15c, and with a slight grain rotation, the actual Schmid factor of this slip system can increase greatly. This specific case appeared to happen to create faceted grains in the two HCF fracture surface shown in Figs. 11 and 12. As shown in the figures, the facets are parallel to (-111) slip planes in both samples. The measured angle between loading direction and facet normal is ~35° and the deviation from ideal Goss orientation is ~ 5° (see the faceted grain in Fig. 11) in the first HCF sample and ~7° in the second sample (see faceted grain or Grain 1 in Fig. 12e). As a result, the Schmid factor for the (-111)[101] slip system in the Goss grains increased from 0.408 to 0.45 and 0.49, respectively in the two samples.

The requirement of high Schmid factor for slip system activation and the formation of crystallographic facets has been proposed not only in nickel-based superalloys [35], but in other engineering alloys such as titanium alloys [36]. Recently, much of attention has been paid to the correlation between facet (plane) formation and grain orientation or microtexture in Ti–6Al–4V alloy, and generally believe that facet cracks preferentially form in grain oriented with a c-axis miorientation between 15° and 40° from loading direction. Dislocations along slip systems with highest Schmid factor and mirocrack induced by the slip have also been observed using transmission electron microscope (TEM) [36]. In studying the VHCF in a polycrystalline nickel-based superalloy, Miao *et.al* [35] observed that slip plane with highest resolved shear stresses is parallel to both the facet plane and the Σ3 twin boundary, suggesting that one of two criteria for facet formation is slip plane with high Schmid factor parallel to twin boundary.

It was evident from the current study, that the crack initiated in a grain that possesses highest average Schmid Factor value among surrounding grains. Comparing three observed grains in Fig. 12d, *i.e.*, Grain 1, Grain 2, Grain 3, it appears that in addition to the higher value of Schmid factor of favorable activated slip system in faceted grain (0.49 in Grain 1) compared to the Grain 2 and Grain 3 (0.46 and 0.45 in Grain 2 and Grain 3, respectively), the Schmid factor of other available not-activated slip systems in Grain 1 (0.47, 0.36 and 0.26) are much greater than in Grain 2 and Grain 3 (0.41, 0.14, 0.03 in Grain 2 and 0.44, 0.09, 0.06 in Grain 3). Moreover, within the faceted grain, the crack occurred on a {111}<1-10> octahedral slip with a highest Schmid factor value among all the available slip system. Here, in Grain 1, the Schmid factor of 2nd rank favorable slip system (0.47) is slightly smaller than the 1st rank activated slip system (0.49). It should be noted that the Schmid factor calculation here is based on the validity of the external uniaxial stress state within individual grains without considering additional local stresses. Although it has been reported that the effective Schmid factors might be affected by local stress states which maybe generated by a present of precipitates such as carbides, adjacent grains or residual stress [37]. However, as discussed previously, the carbides in HCF failed areas were relatively small and homogeneously distributed. Moreover, it should be noted that the microstructure of the failed HCF specimens consist of very large size grains (order of mm), where the entire fracture surface consists of only two and three grains along ND direction as shown in Fig. 11 and Fig. 12, respectively. Furthermore, in the current study, most of the Schmid factor calculations matched well with the effective slip plane (faceted plane). Therefore, the local stress effect is likely to be negligible in this study. It has also been reported [38] that at relatively small plastic strains under fatigue conditions, the crystalline interaction does not essentially affect the local stress within the grains. Nevertheless, high Schmid factor value alone may not sufficient for dislocation accumulation and slip system activation if cyclic stress level is relatively low. In that case, casting defects such as porosities can provide stress concentration zone and lead to cyclic plastic strain localisation, which further lead to the accumulation of dislocations along slip plane and eventually microcracks formation.

Based on the 3D serial sectioning observations in Figs. 11 and 12, two schematic models for crack initiation, facets formations and crack propagation mechanisms are presented in Figs. 15 e and f. As discussed and demonstrated in Fig. 15a and Fig. 3, there are three stages during HCF failure, that is, crack initiation stage characterised as facet (Fig. 3c), crack propagation stage characterised as striation (Fig. 3b) and mechanical rupture stage of tensile overload (Fig. 3a). The main difference between the two failure models in Fig. 15 is strongly dependant on the microstructure cluster. The first failure mode observed on a fracture surface with only two grains demonstrate the fracture mode observed in Fig. 11 and schematically presented in Fig. 15e, the second fracture mode represent a HCF failure crack within multi-grain cluster as presented in Fig. 15f and demonstrated in Fig. 12b. It appears that the direct effect of grain size on fatigue crack formation is the size of the facet. As demonstrated in Fig. 15e-f, the radial dimension of the facet along Normal Direction (ND) is the same length of the grain diameter (grain 1 in Fig. 15 e and f). This clearly demonstrates that the crystallographic facet in a favourably oriented grain for octahedral slip system activation can provide unrestricted slip plane and an easy crack propagation until reaching the grain boundary and encountering neighbouring grains. In addition, the most distinguished fatigue crack feature is that in mode 1 with large grain size, the crack initiation and propagation areas are both confined in the same grain, see grain 1 in Fig. 15e. Whilst in mode 2 with smaller grains, the crack initiates and grows in Grain 1 (high Schmid Factor) and propagates through encountering neighbouring grain (Grain 3), due to the impediment effect and crack propagation resistance from Grain 2 (low Schmid Factor Brass oriented grain). It is clear that microstructure cluster, *i.e.*, the orientations and microtexture of the grain cluster (surrounding grains around crack initiation plane), have a great effect on fatigue initiation and propagation during HCF failure. Thus, the microstructure cluster can play a vital role in crack acceleration or retardation depending on the cluster configuration of hard and soft grains.

5. Conclusion:

Based on detailed microstructure/microtexure analysis and fractography observations of failed turbocharger wheel blades during in-house LCF and HCF tests, together with strain mapping and GND density calculation via high-resolution EBSD, distinct deformation and failure mechanism for LCF and HCF are proposed and influence of predominant internal structure heterogeneity in terms of carbides, dendrite and grain orientation are demonstrated and verified.

1. Different fatigue cracks initiation and propagation mechanisms for LCF and HCF of wheel blades during in-house tests are established. The failure mechanism was greatly affected by loading conditions, microstructure and geometrical factor of wheel blades.
2. HCF failure usually occurred on the upper position of turbine wheel blades and the fracture surface features consist of facet, beach marks and clearly-defined striations. Whilst LCF failure occurred on the surface of blade root where highest stress concentration exists and numbers of secondary cracks and dendrite structure can be found close to the crack initiation sites.
3. The microstructures across the turbine wheel blades is not homogenous due to different cooling rate along the blade during investment casting process. In upper position of blades, relatively uniform microstructure is produced with weak dendrite structure as well as fine and evenly distributed carbides. Whilst in the blade root area, well connected dendrite network with larger dendrite arm size and large cluster-like carbides are observed.
4. During LCF, once cracks initiated due to high applied stress level, cracks propagated via oxidised carbides paths, and the connecting structure of carbides in the lower location of the

blade facilitated the failure process. In the later stage of cracks propagation, the weakened interdendrite area rotate to accommodate the increased plastic strain during loading, leading to the hard grain fragmentation and catastrophic failure.

5. The effect of carbides and interdendrite morphology on LCF failure mechanism are examined by GND distribution and evolution. Higher GND density was found around carbides than in γ matrix, and greater values in interdendrite than in dendrite areas. A very high GND density was found at the tip of oxidised carbides and ahead/tip of small cracks due to volume expansion during oxidation process.
6. During HCF, the crack initiations are determined by grain orientations, microstructure cluster and casting defects. It is observed that most of the facet formed on {111}<1-10> slip system with highest Schmid factor values. Moreover, the cracks initiation during HCF test was defect-sensitive and an easy slip system activation for a slip plane with high Schmid factor is assisted by the presence of porosity.
7. The size of facet is limited by grain size. It is concluded that the number, size and distribution of the grains surrounding facet grain have a great effect on the crack propagation path.
8. Depending on different fatigue initiation and propagation mechanisms in LCF and HCF proposed in this study, it is recommended that LCF resistance for turbine wheel blade can be increased by microstructure modification such as reducing carbides size, disrupting carbide network and connectivity. Whilst for HCF resistance it is highly recommended to reduce the casting defects and controlling the microstructure/microtexture clusters in order to retard crack propagation.

Acknowledgements

The authors would like to thank CSC (Chinese Scholarship Council) and College of Engineering in Swansea University for the project funding. Special thanks to Dr. Yong Li at Swansea University for the useful discussion throughout this project.

References

[1] H. Matysiak, M. Zagorska, A. Balkowiec, B. Adamczyk-Cieslak, R. Cygan, J. Cwajna, J. Nawrocki, K.J. Kurzydłowski, The microstructure degradation of the IN 713C nickel-Based Superalloy after the stress rupture tests, J. Mater. Eng. Perform. 23(9) (2014) 3305-3313.

[2] M. Coleman, H. Alshehri, R. Banik, W. Harrison, S. Birosca, Deformation mechanisms of IN713C nickel based superalloy during Small Punch Testing, Mater. Sci. Eng. A 650 (2016) 422-431.

[3] D. Gelmedin, K.-H. Lang, Fatigue behaviour of the superalloy IN 713C under LCF-, HCF- and superimposed LCF/HCF-loading, Procedia Engineering 2(1) (2010) 1343-1352.

[4] L. Kunz, P. Lukáš, R. Konečná, High-cycle fatigue of Ni-base superalloy Inconel 713LC, Int. J. Fatigue 32(6) (2010) 908-913.

[5] L. Kunz, P. Lukáš, R. Konečná, S. Fintová, Casting defects and high temperature fatigue life of IN 713LC superalloy, Int. J. Fatigue 41 (2012) 47-51.

[6] M. Petrenec, K. Obrtlík, J. Polák, Inhomogeneous dislocation structure in fatigued INCONEL 713 LC superalloy at room and elevated temperatures, Mater. Sci. Eng. A 400-401 (2005) 485-488.

[7] N. Boutarek, D. Saïdi, M.A. Acheheb, M. Iggui, S. Bouterfaïa, Competition between three damaging mechanisms in the fractured surface of an Inconel 713 superalloy, Mater. Charact. 59(7) (2008) 951-956.

[8] M. Goto, D. M. Knowles, Initiation and propagation behaviour of microcracks in Ni-base superalloy Udimet 720 Li, Eng. Fract. Mech. 60(1) (1998) 1-18.

[9] Z.K. Chu, J.J. Yu, X.F. Sun, H.R. Guan, Z.Q. Hu, High cycle fatigue behavior of a directionally solidified Ni-base superalloy DZ951, Mater. Sci. Eng. A 496(1–2) (2008) 355-361.

[10] H.S. Kitaguchi, H.Y. Li, H.E. Evans, R.G. Ding, I.P. Jones, G. Baxter, P. Bowen, Oxidation ahead of a crack tip in an advanced Ni-based superalloy, Acta Mater. 61(6) (2013) 1968-1981.

[11] T. Connolley, P.A.S. Reed, M.J. Starink, Short crack initiation and growth at 600 °C in notched specimens of Inconel718, Mater. Sci. Eng. A 340(1–2) (2003) 139-154.

[12] A. Pineau, D.L. McDowell, E.P. Busso, S.D. Antolovich, Failure of metals II: Fatigue, Acta Mater. 107 (2016) 484-507.

[13] P. Kontis, E. Alabort, D. Barba, D.M. Collins, A.J. Wilkinson, R.C. Reed, On the role of boron on improving ductility in a new polycrystalline superalloy, Acta Mater. 124 (2017) 489-500.

[14] P. Kontis, D.M. Collins, A.J. Wilkinson, R.C. Reed, D. Raabe, B. Gault, Microstructural degradation of polycrystalline superalloys from oxidized carbides and implications on crack initiation, Scr. Mater. 147 (2018) 59-63.

[15] S. Birosca, F. Di Gioacchino, S. Stekovic, M. Hardy, A quantitative approach to study the effect of local texture and heterogeneous plastic strain on the deformation micro-mechanism in RR1000 nickel-based superalloy, Acta Mater. 74 (2014) 110-124.

[16] M. Calcagnotto, D. Ponge, E. Demir, D. Raabe, Orientation gradients and geometrically necessary dislocations in ultrafine grained dual-phase steels studied by 2D and 3D EBSD, Mater. Sci. Eng. A 527(10) (2010) 2738-2746.

[17] P.S. Karamched, A.J. Wilkinson, High resolution electron back-scatter diffraction analysis of thermally and mechanically induced strains near carbide inclusions in a superalloy, Acta Mater. 59(1) (2011) 263-272.

[18] T. Benjamin Britton, A.J. Wilkinson, Stress fields and geometrically necessary dislocation density distributions near the head of a blocked slip band, Acta Mater. 60(16) (2012) 5773-5782.

[19] J. Jiang, J. Yang, T. Zhang, J. Zou, Y. Wang, F.P.E. Dunne, T.B. Britton, Microstructurally sensitive crack nucleation around inclusions in powder metallurgy nickel-based superalloys, Acta Mater. 117 (2016) 333-344.

[20] J. Jiang, J. Yang, T. Zhang, F.P.E. Dunne, T.B. Britton, On the mechanistic basis of fatigue crack nucleation in Ni superalloy containing inclusions using high resolution electron backscatter diffraction, Acta Mater. 97 (2015) 367-379.

[21] J. Nye, Some geometrical relations in dislocated crystals, Acta Metall. 1(2) (1953) 153-162.

[22] M. Ashby, The deformation of plastically non-homogeneous materials, Philos. Mag. 21(170) (1970) 399-424.

[23] A. Arsenlis, D. Parks, Crystallographic aspects of geometrically-necessary and statistically-stored dislocation density, Acta Mater. 47(5) (1999) 1597-1611.

[24] W. He, W. Ma, W. Pantleon, Microstructure of individual grains in cold-rolled aluminium from orientation inhomogeneities resolved by electron backscattering diffraction, Mater. Sci. Eng. A 494(1-2) (2008) 21-27.

[25] A.J. Wilkinson, D. Randman, Determination of elastic strain fields and geometrically necessary dislocation distributions near nanoindents using electron back scatter diffraction, Philos. Mag. 90(9) (2010) 1159-1177.

[26] J. Jiang, T.B. Britton, A.J. Wilkinson, Measurement of geometrically necessary dislocation density with high resolution electron backscatter diffraction: Effects of detector binning and step size, Ultramicroscopy 125 (2013) 1-9.

[27] T.M. Pollock, S. Tin, Nickel-based superalloys for advanced turbine engines: chemistry, microstructure, and properties, J. Propul. Power 22(2) (2006) 361-374.

[28] F.P.E. Dunne, A.J. Wilkinson, R. Allen, Experimental and computational studies of low cycle fatigue crack nucleation in a polycrystal, Int. J. Plast 23(2) (2007) 273-295.

[29] L. Engel, H. Klingele, An atlas of metal damage, Wolfe Publishing Ltd. (1981) 271.

[30] A. Bhambri, T. Kattamis, J. Morral, Cast microstructure of Inconel 713C and its dependence on solidification variables, Metall. Trans. B 6(4) (1975) 523-537.

[31] J. Jiang, T. Britton, A. Wilkinson, Evolution of dislocation density distributions in copper during tensile deformation, Acta Mater. 61(19) (2013) 7227-7239.

[32] A.N. Stroh, A theory of the fracture of metals, Adv. Phys. 6(24) (1957) 418-465.

[33] V.V.C. Wan, J. Jiang, D.W. MacLachlan, F.P.E. Dunne, Microstructure-sensitive fatigue crack nucleation in a polycrystalline Ni superalloy, Int. J. Fatigue 90 (2016) 181-190.

[34] L.G. Zhao, J. Tong, M.C. Hardy, Prediction of crack growth in a nickel-based superalloy under fatigue-oxidation conditions, Eng. Fract. Mech. 77(6) (2010) 925-938.

[35] J. Miao, T.M. Pollock, J.W. Jones, Crystallographic fatigue crack initiation in nickel-based superalloy René 88DT at elevated temperature, Acta Mater. 57(20) (2009) 5964-5974.

[36] I. Bantounas, D. Dye, T.C. Lindley, The role of microtexture on the faceted fracture morphology in Ti–6Al–4V subjected to high-cycle fatigue, Acta Mater. 58(11) (2010) 3908-3918.

[37] P. Peralta, C. Laird, Fatigue fracture at bicrystal interfaces: experiment and theory, Acta Mater. 46(6) (1998) 2001-2020.

[38] C. Blochwitz, J. Brechbühl, W. Tirschler, Analysis of activated slip systems in fatigue nickel polycrystals using the EBSD-technique in the scanning electron microscope, Mater. Sci. Eng. A 210(1) (1996) 42-47.

Table Captions:

Table 1 IN731C chemical composition (wt.%).

Table 1 IN731C chemical composition (wt.%)

Ni	Cr	Al	Mo	Nb+Ta	Ti	C	Zr	B
Bal	12.50	6.10	4.20	2.20	0.80	0.12	0.10	0.01

Table 2 Segregation ratio and composition of elements in dendrtite structure of the LCF failed specimen.

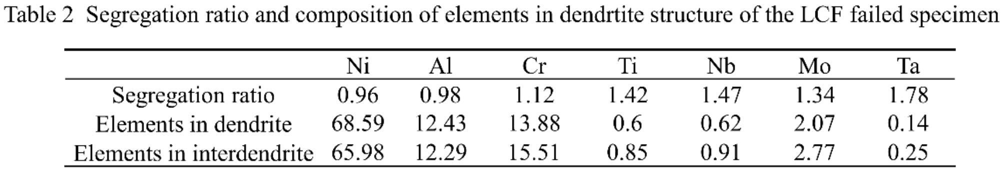

Table 2 Segregation ratio and composition of elements in dendrtite structure of the LCF failed specimen

	Ni	Al	Cr	Ti	Nb	Mo	Ta
Segregation ratio	0.96	0.98	1.12	1.42	1.47	1.34	1.78
Elements in dendrite	68.59	12.43	13.88	0.6	0.62	2.07	0.14
Elements in interdendrite	65.98	12.29	15.51	0.85	0.91	2.77	0.25

Table 3 Schmid factors for slip systems in four typical grain orientations.

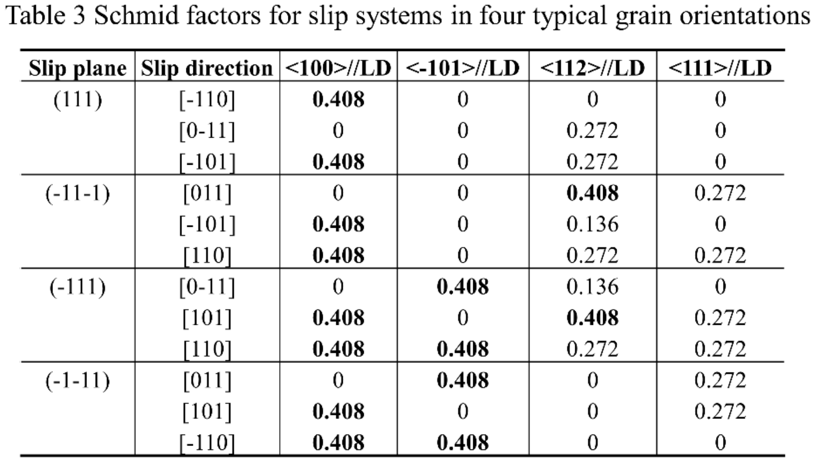

Table 3 Schmid factors for slip systems in four typical grain orientations

Slip plane	**Slip direction**	**<100>//LD**	**<-101>//LD**	**<112>//LD**	**<111>//LD**
(111)	[-110]	**0.408**	0	0	0
	[0-11]	0	0	0.272	0
	[-101]	**0.408**	0	0.272	0
(-11-1)	[011]	0	0	**0.408**	0.272
	[-101]	**0.408**	0	0.136	0
	[110]	**0.408**	0	0.272	0.272
(-111)	[0-11]	0	**0.408**	0.136	0
	[101]	**0.408**	0	**0.408**	0.272
	[110]	**0.408**	**0.408**	0.272	0.272
(-1-11)	[011]	0	**0.408**	0	0.272
	[101]	**0.408**	0	0	0.272
	[-110]	**0.408**	**0.408**	0	0

Figure Captions:

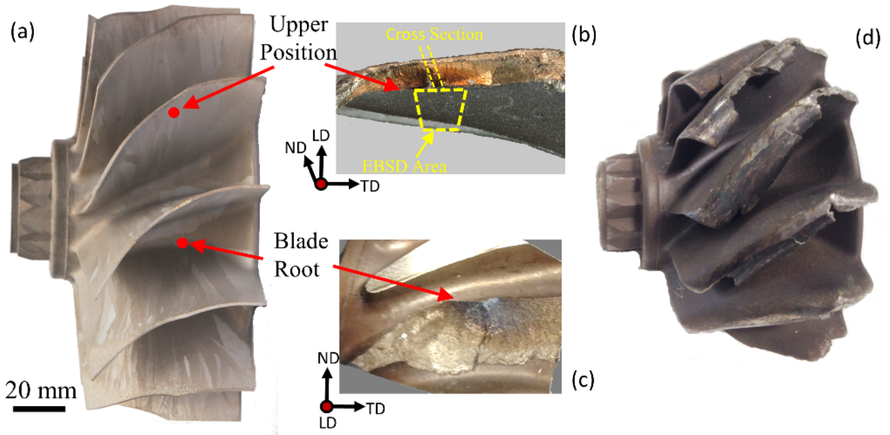

Fig. 1 Turbine wheel blade prior (a) and post (d) testing at 600ºC, typical failure location during HCF (b) and LCF (c) tests.

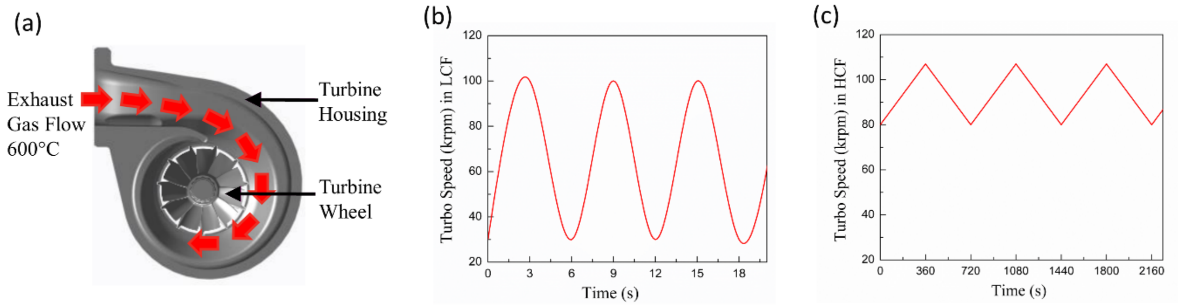

Fig. 2 Test schematic for LCF and HCF test (a) and turbo speed versus time during LCF (b) and HCF (c) tests. By changing turbo speed range and inner turbine housing structure, wheel blade failed by resonance in HCF test.

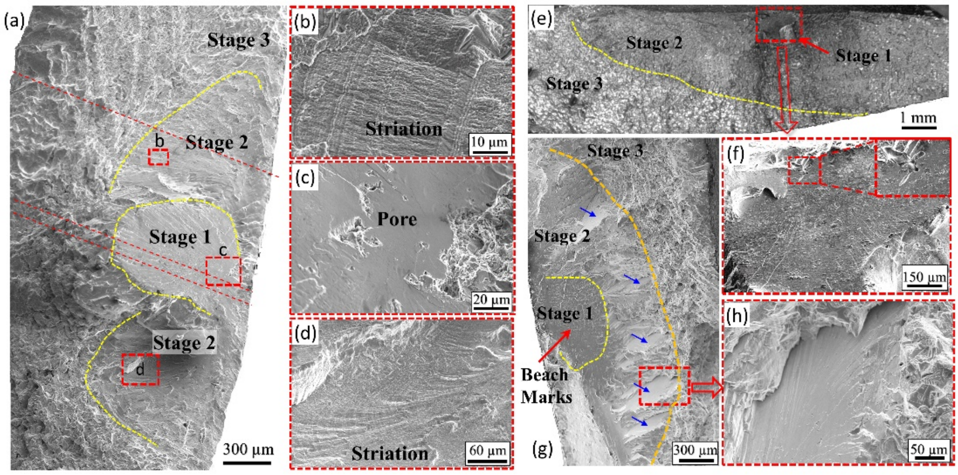

Fig. 3 Typical fractography of HCF test specimen. Three failed specimens are shown here. (a-d) Specimen 1, (e, f) Specimen 2, and (g, h) Specimen 3. ((b,c,d) are magnified image in red rectangular areas in (a). (f) and (h) are magnified images in red rectangular areas in (e) and (g), respectively. Three stages of crack initiation and propagation are indicated.

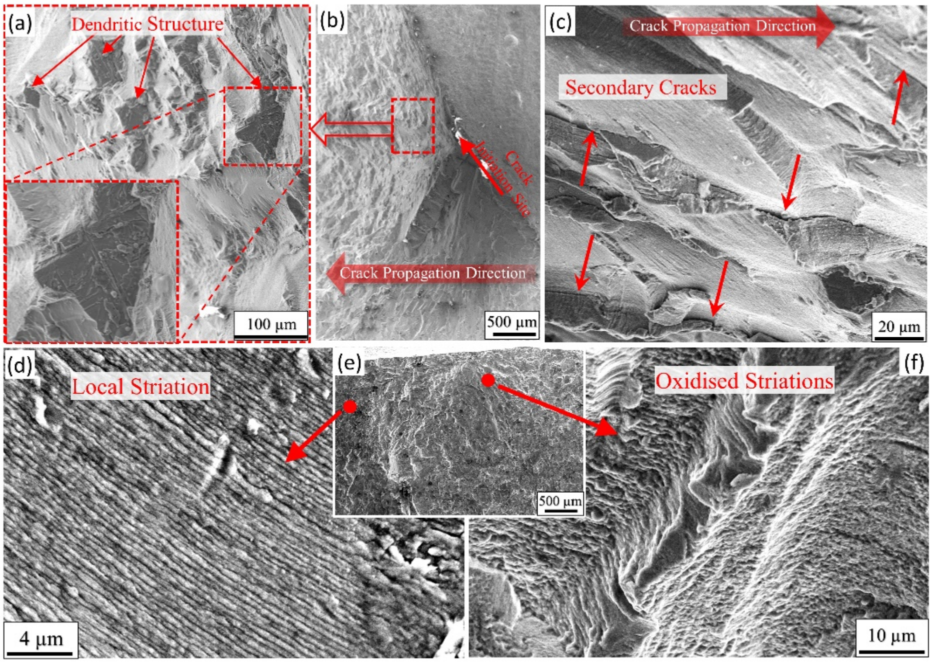

Fig. 4 Fractography of 3 LCF test specimens. (a, b) Specimen 1, (c) Specimen 2, and (d-f) Specimen 3. (a) Magnified image of the red rectangular area in (b) showing dendritic structure close to initiation site. (b) Crack initiation site and propagation area in Specimen 1. (c) secondary cracks close to initiation site in Specimen 2. (d) local striations in propagation area in the Specimen 3 (e), (f) oxidised striations close to initiation site in (e).

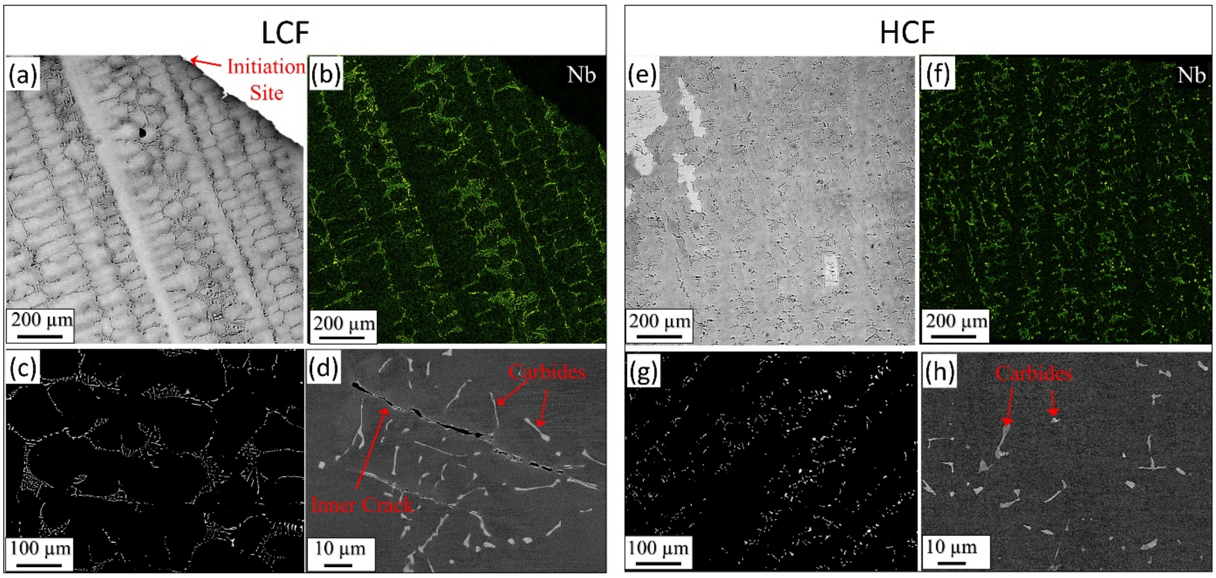

Fig. 5 SEM images of Dendritic structure (a, e), optical micrographs of carbide network (c, g) and carbides size and morphology (d, h) in LCF and HCF failed specimens. Nb EDX maps for the area in (a, e), shown in (b, f), respectively, to signify the Nb element partition in dendritic structure.

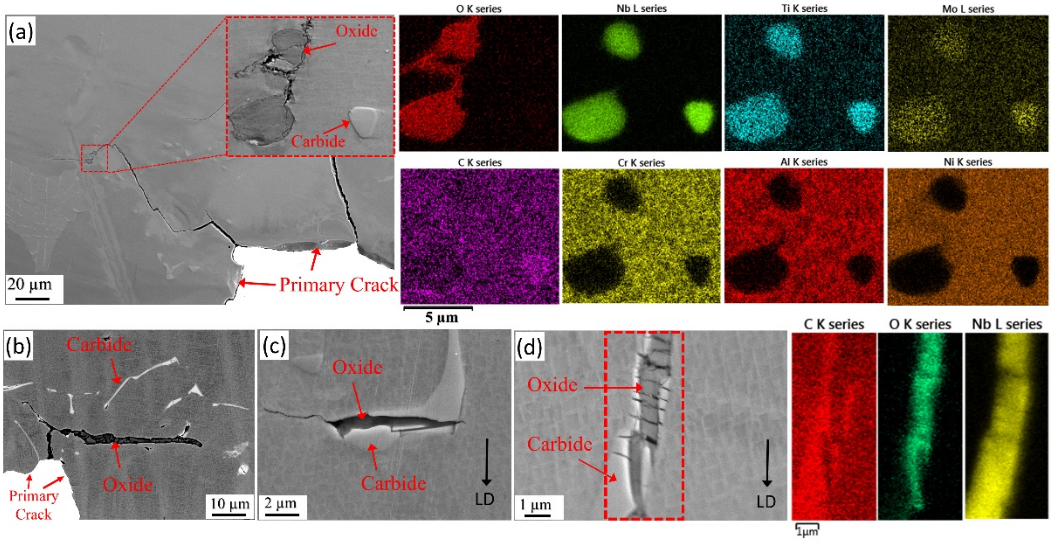

Fig. 6 Typical oxides and semi-transformation of oxides from carbides in LCF failed specimen. (a) oxides change the second crack propagation direction and EDS maps show the chemical composition of red dashed rectangular area in the left; (b) second crack initiated from oxides; (c) inner short crack initiated from oxide and (d) semi-transformation of oxides from carbides with EDS maps for the red dashed rectangular area in (d).

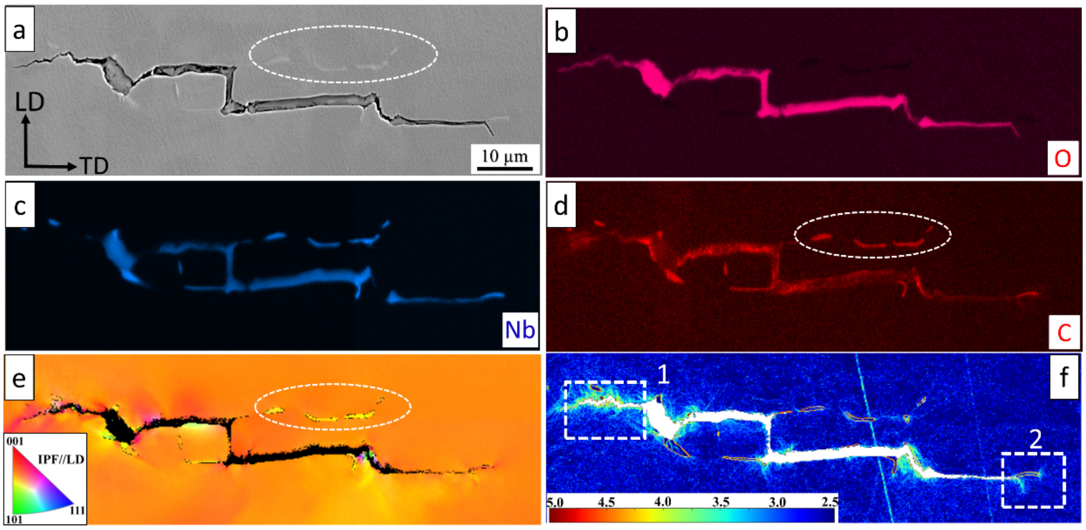

Fig. 7 Near surface oxidised carbides in LCF failed specimen. (a) SE image of carbides and oxidized carbides; (b-d) selected EDS mapping for elements C, O and Nb in area (a); (e) EBSD-derived IPF//LD map of area (a); (f) GND (Geometrically Necessary Dislocation) map with step size of 200 nm.

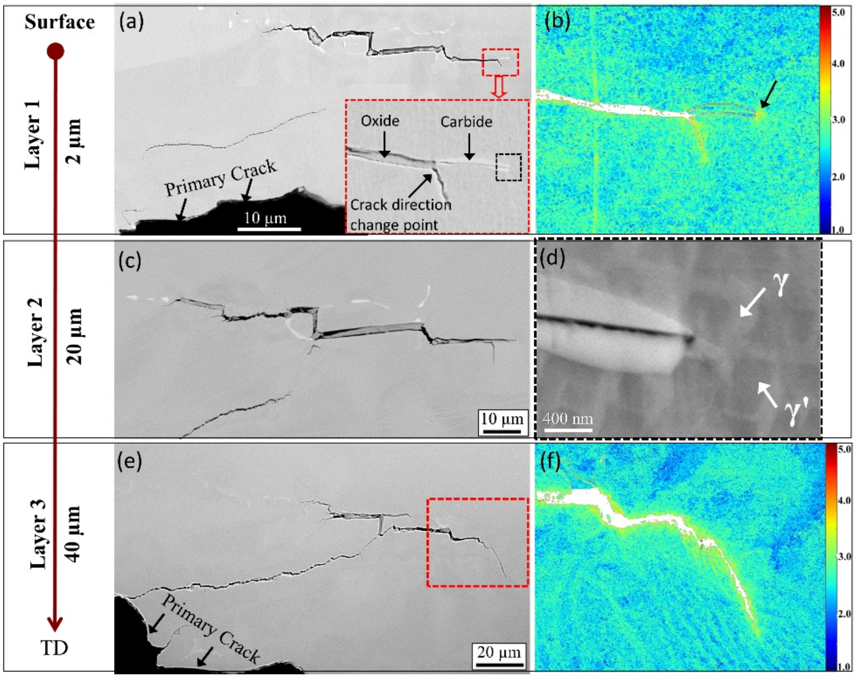

Fig. 8 Three layer of the same area GND density maps in LCF failed specimen. (a), (c) and (e) are SE or BSE images; (b) and (f) are high-resolution GND maps with step size of 60 nm in the red

rectangular area in (a) and (e), respectively; (d) is the GND map for (c); the inset of (b) is the same area of black rectangular area in (a), showing the γ’ impeding carbide.

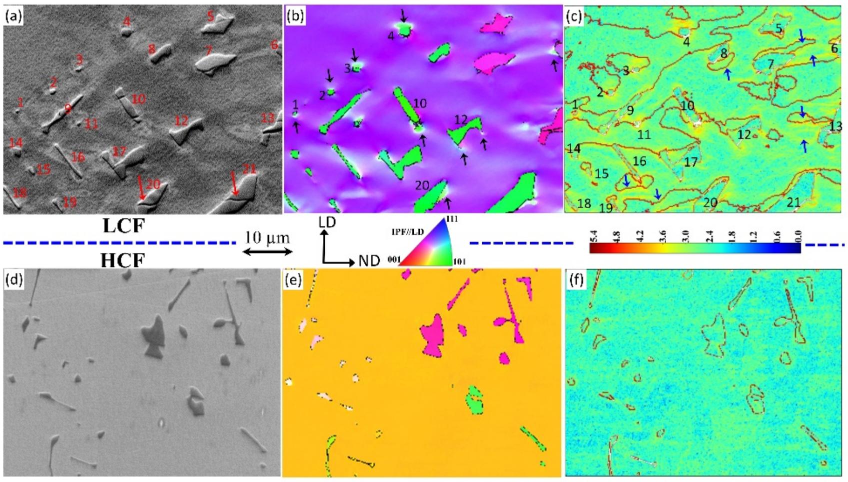

Fig. 9 GND density and their local distribution of carbides near crack initiation sites in LCF (a-c) and HCF (d-f) failed specimens. (a,d) SEM image; (b, e) EBSD-derived IPF//LD; (d,f) GND density maps using step size of 200 nm.

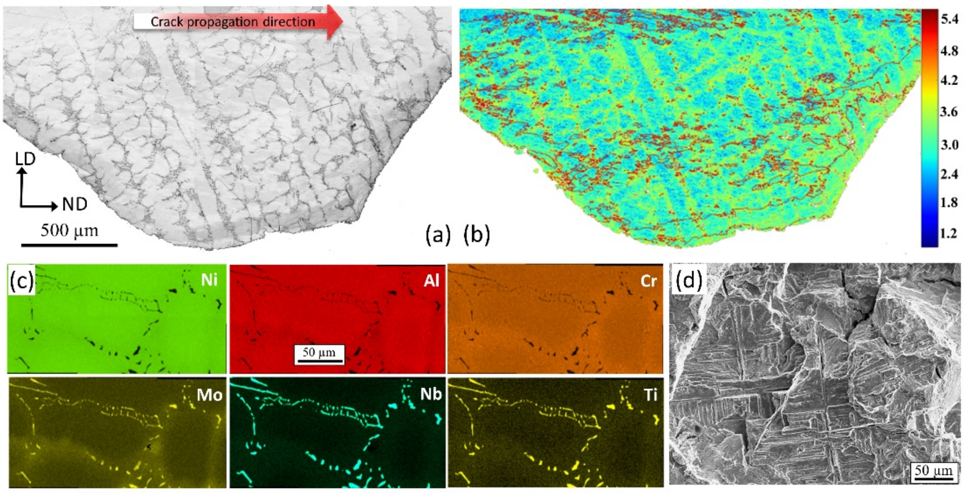

Fig. 10 GND density distribution in dendritic structure in LCF failed specimen. (a) Band contrast image of large area of interest; (b) GND density map for the same area in (a) with step size of 0.5µm; (c) fracture surface in crack propagation area revealing sharp and square shape dendritic structure and (d) EDS chemical elements maps for a selected area in (a).

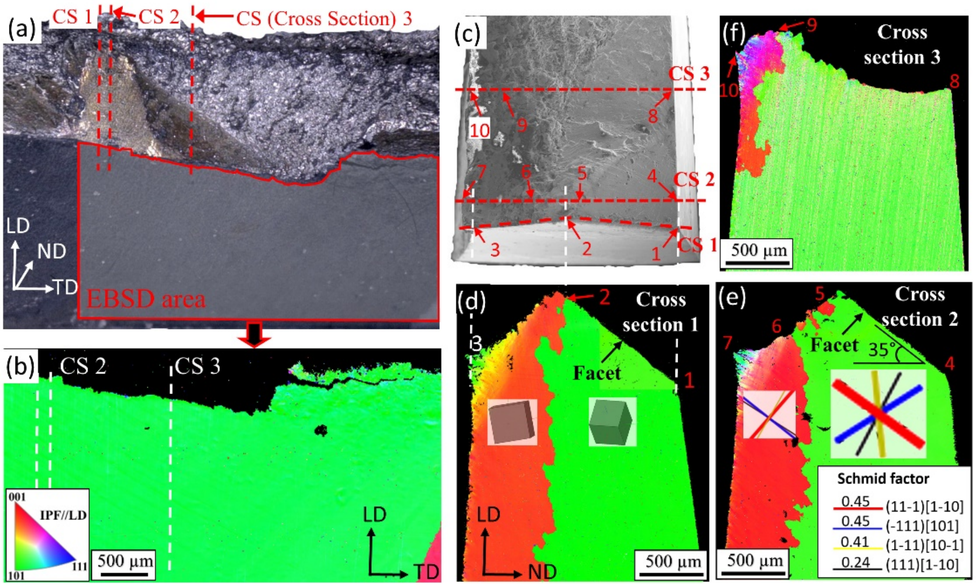

Fig. 11 EBSD-derived IPF//LD across facet after serial sectioning on a HCF failed fracture surface. Sectioning position are indicated in dashed lines in (a,b,c), and are the same position indicated in red dashed lines in Fig. 3a. (d,e,f) are IPFs map //LD of cross section 1-3, respectively, parallel to LD-ND plane, and (b) is IPF//LD of LD-TD plane indicated as red line enclosed area in (a). {111} Slip traces and 3D-view of crystal are superimposed on IPF maps in (e) and (d). Schmid factor values for each slip system in facet grain are listed in the inset of (e).

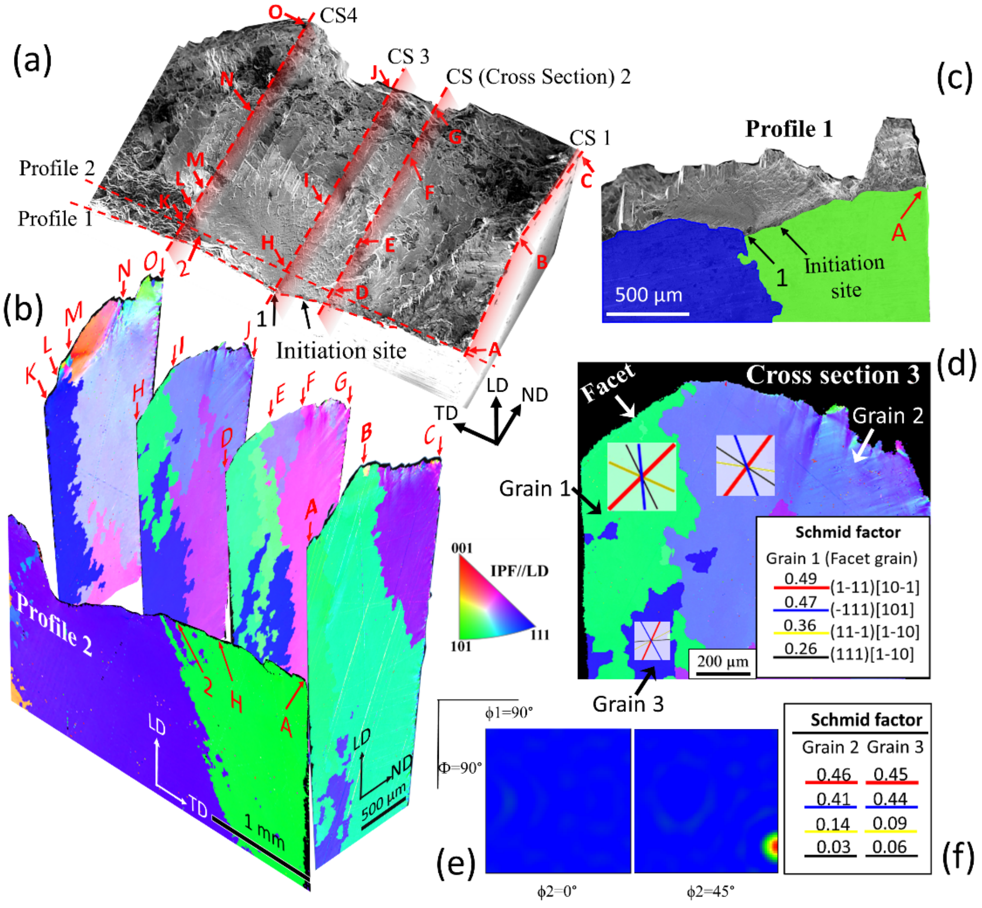

Schmid factor

Grain 1 (Facet grain)

Schmid factor	Slip system
0.49	(1-11)[10-1]
0.47	(-111)[101]
0.36	(11-1)[1-10]
0.26	(111)[1-10]

Schmid factor

Grain 2	Grain 3
0.46	0.45
0.41	0.44
0.14	0.09
0.03	0.06

Fig. 12 3-D view of the microstructure, grain orientations around a facet for a HCF failed specimen. (a) SE-SEM image of the fracture surface; the section direction along ND (CS) and TD (profile) are indicated in red dashed lines.; (b) selected EBSD-derived IPF of Cross Sections (CS) on and near facet plane. (c) IPF//LD of the section plane parallel to LD-TD plane (profile 1), IPF//LD of profile 2 are shown in (b); (d) part of IPF//LD of cross section 3 on facet grain. Slip trace maps for three grains (Grain 1-3) are superimposed on the IPF. (e) ODF (Orientation Distribution Function) of facet grain (Grain 1); Schmid factor values are for three grains listed in (d) and (f).

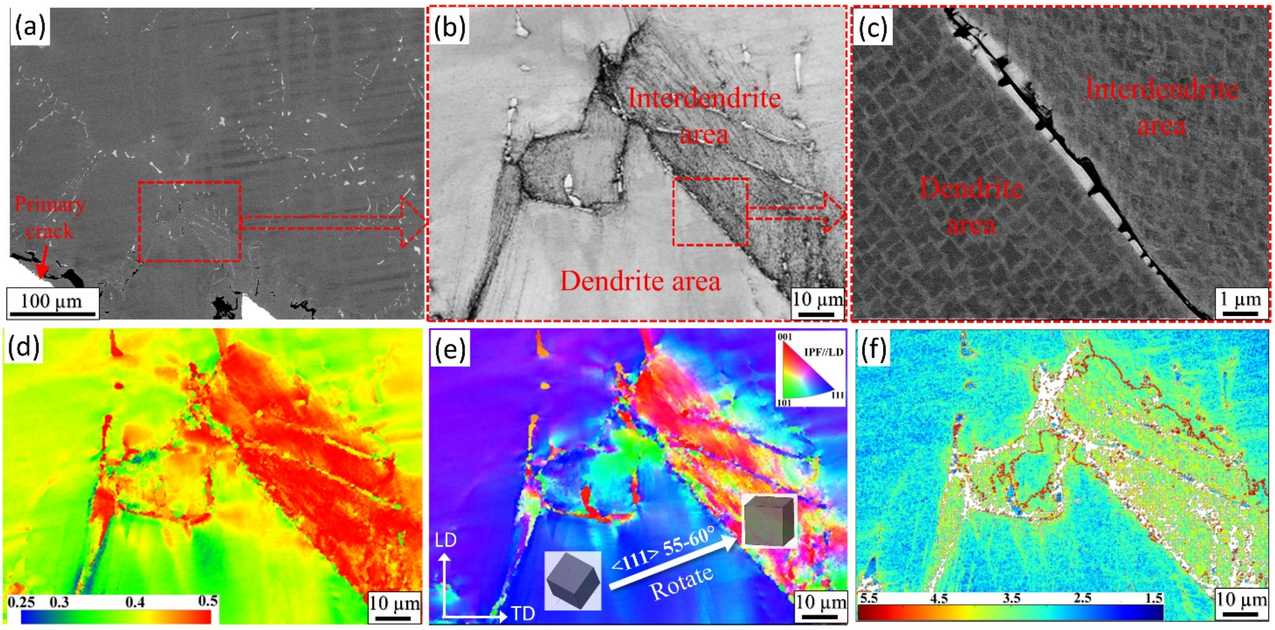

Fig. 13 Illustration of dendritic weakening during LCF failure. (a) Low magnification image shows the dendritic structure, (b) Band Contrast (BC) map of the red rectangular area in (a); (c) SE image of the red rectangular area in (b) showing the γ’ structure in dendrite and interdendrite areas; (d) Schmid factor map, (e) EBSD-derived IPF//LD and (f) calculated GND density map of area in (b) with step size of 300 nm.

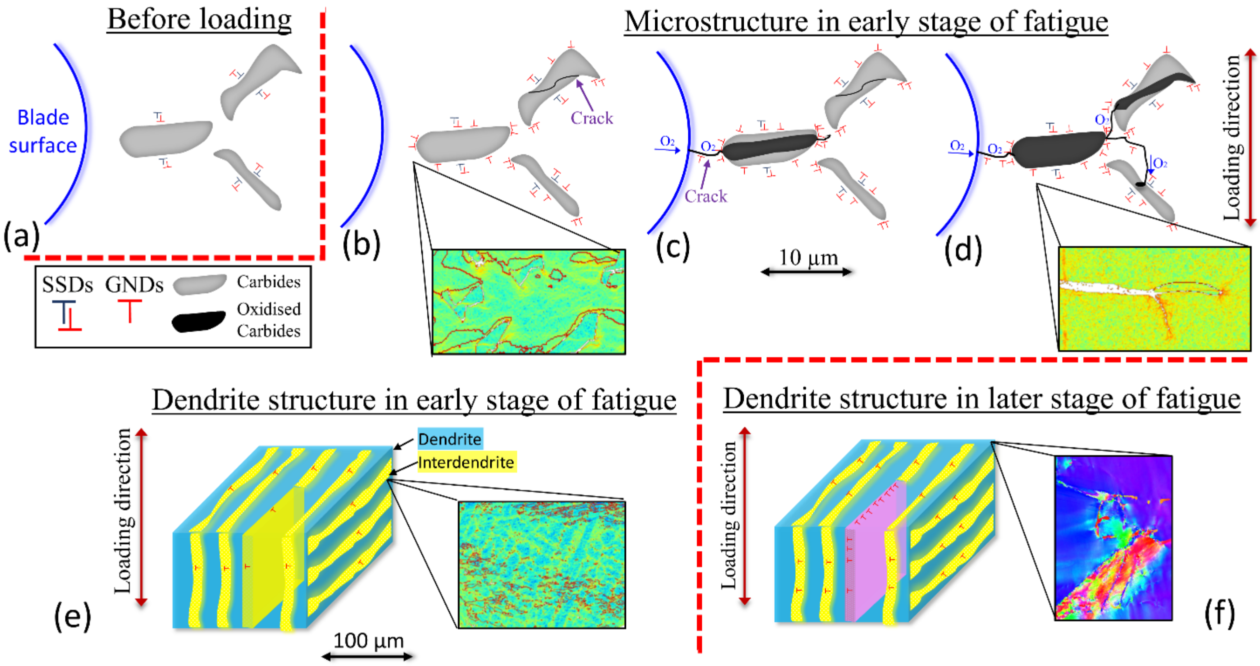

Fig. 14 Schematic showing the failure mechanism of crack initiation and propagation in the early (b-d) and later (f) stage of LCF test, and the effects of both carbides/oxides (microscopically, b-d) and (dendrite structure e-f) on crack initiation and propagation process.

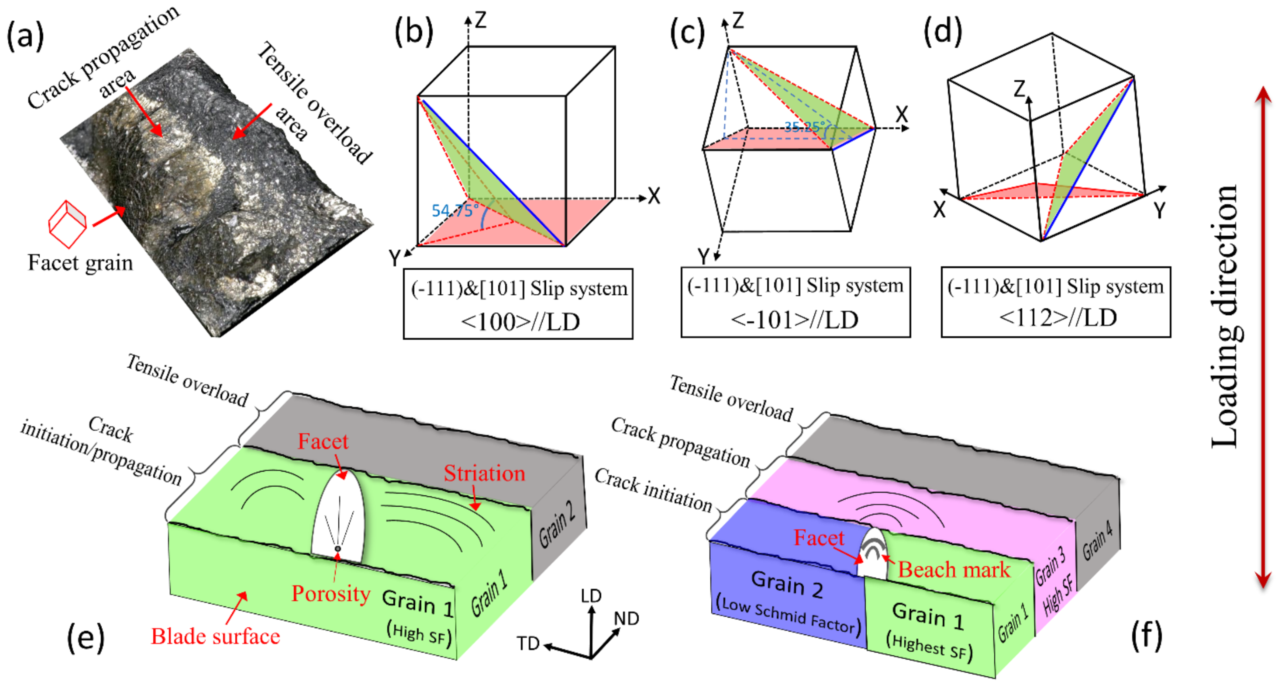

Fig. 15 Schematic showing the failure mechanism of crack initiation and propagation during HCF test. (a) a fracture surface of a failed sample, showing facet formation and rack propagation stages. (b-d) ideal facet plane orientation in different orientations. (111)<110> slip system with high Schmid factor (0.408) in <100>//LD, <110>//LD and <112>//LD grains are shown. Red planes are normal plane to loading direction (LD) and green planes are {111} slip planes with high Schmid factor. (e) and (f) two macroscopical fracture modes during HCF test, note the number, size, structure of grains and their correlation with crack stages in two modes.